ORIGINAL PAPER

Folic acid-conjugated chromium(III) doped nanoparticles consisting of mixed oxides of zinc, gallium and tin, and possessing near-infrared and long persistent phosphorescence for targeted imaging of cancer cells

Yang Li[1] · Ruchun Chen[1] · Yiyang Li[2] · Kaniyarakkal Sharafudeen[3] ·
Shijian Liu[1] · Dakun Wu[1] · Yiling Wu[1] · Xixi Qin[1] · Jianrong Qiu[1]

Abstract Folic acid-conjugated luminescent nanomaterials have long been widely used in targeted bioimaging, often simultaneously acting as vehicles for drug delivery. They often require, however, intense light sources for photoexcitation, and this often results in photobleaching, strong luminescence background, and strong light scattering. This article describes the preparation of nanoparticles (NPs) of the type $Zn_{1.1}Ga_{1.8}Sn_{0.1}O_4$ doped with Cr(III) ions and surface-modified with folic acid. The functionalization of the NPs was monitored via measurement of zeta potentials, FTIR spectra and thermogravimetry. Cell viability and biocompatibility were tested using the MTT kit. The NPs have a size of 220 nm and were characterized by dynamic X-ray diffraction, light scattering, field emission scanning electron microscopy and high-resolution transmission electron microscopy. After annealing the NPs for 10 min at 300 °C and irradiating them with 254 nm light for 10 min, they display deep red emission that persists for up to 10 h. The NPs are easily dispersed, small-sized, and crystalline. In our perception, the new material with its long decay time offers quite novel features in terms of targeted optical imaging in providing high resolution, weak disturbance by background luminescence, and the absence of light scattering. They were successfully applied to image MCF-7 and A549 cells.

Introduction

Today cancer has become one of the leading causes for death [1]. It is generally recognized now that the detection of tumor cells at an early stage represents a most powerful weapon against cancer [2]. The coincident developments of nanomaterials, biomedicine and imaging techniques have provided unprecedented opportunities for addressing many challenges in cancer tracing and assessment [3]. Targetable near-infrared (NIR) nanoparticles are expected to be an almost ideal and robust expression vector. It can establish advanced optical imaging with high resolution and weak light disturbance features for realistic analysis of the structural and functional processes in cells, tissues and other complex systems [4].

Many efforts to develop tumor-specific nanoprobes have focused on the synthesis of targeting ligands-conjugated nanomaterials, which will efficiently bind the receptors overexpressed on cancer cells [5]. Folic acid (FA) has emerged as an attractive specific ligand for targeted cancer imaging, because folate receptors (FRs) are the highly selective tumor probes

✉ Jianrong Qiu
qjr@scut.edu.cn

Yang Li
msliyang@scut.edu.cn

1 State Key Laboratory of Luminescent Materials and Devices, School of Materials Science and Technology, South China University of Technology, Guangzhou 510640, China

2 Henry Samueli School of Engineering, University of California, Irvine, CA 92697-2575, USA

3 Escola de Engenharia de Sao Carlos, Universidade de Sao Paulo, 13566-590 Sao Carlos, SP, Brazil

overexpressed in many of the human cancerous cells, such as, endometrial, lung, mesothelioma, brain, ovarian and breast carcinomas, etc. [6]. FRs are a kind of cysteine-rich cell-surface glycoproteins that bind FA with high affinity to mediate cellular uptake of FA [3, 7]. Moreover, FA has the advantages of low cost, nonimmunogenic character and ability to conjugate with a wide variety of nanomaterials [8]. To date, the suggested NIR folate-based tracers mainly consist of organic dyes, inorganic semiconducting quantum dots, up and down-conversion luminescent nanoparticles, and noble metal nanoparticles [5, 6, 9–16]. Parts of them have been therapeutically and diagnostically exploited and applied as anti-FR antibodies, high-affinity antifolates, folate-based imaging agents and folate-conjugated drugs and toxins [17, 18]. However, the universal operational mode of today's most advanced examples still involves the harsh requirement of high-level optical excitation, which often yields unexpected photobleaching, background light disturbance, insensitivity, inefficiency, or even photon-induced deterioration and possess limited detection scope during optical imaging.

Therefore, to maximize the signal to noise ratio, researchers have concentrated on a novel delay detection model. It has been suggested that late time-gating (i.e., capturing the signal at a delayed time after exCitation) be applied to guarantee the photo-realistic, high-resolution in vivo imaging [19–21]. In addition to the anticipated advantage of the strongly increased signal to noise ratio, the long phosphorescent phosphors (LPPs), which have the super long afterglow-emission of several minutes or hours after the stoppage of excitation, may overcome the stringent constraint of inherently small beam diameter of excitation source. Thus, the LPPs offer the possibility of rapid, sensitive, stable and efficient optical imaging of tissues over a much larger area [20, 22–25]. Unfortunately, there is no enough work to develop these novel FA-conjugated nanoparticles with near-infrared long persistent phosphorescence.

Here, we designed and synthesized the FA-conjugated $Zn_{1.1}Ga_{1.8}Sn_{0.1}O_4$: Cr^{3+} (FA-ZGSC) nanoparticles with NIR long persistent phosphorescence for targeted fluorescence imaging of cancer cells by a modified sol–gel method. These $Zn_{1.1}Ga_{1.8}Sn_{0.1}O_4$ (ZGSC) nanoparticles showed the easy dispersibility, small-size, good crystallinity, and remarkable long persistent luminescence over 10 h in the near-infrared region, and consequently permitted an enabling long-term, real-time, reliable deep-tissues/cell/in vivo imaging. The surface modification for ZGSC also was demonstrated to assure the function as targeting agents. The cancer cell targeting ability was examined by conducting the uptake of FA-ZGSC nanoparticles by FR-overexpressed MCF-7 cells.

Materials and methods

Materials

Zinc acetate dehydrate, gallium nitrate, tin tetrachloride, chromic nitrate, citric acid, n-butyl alcohol, 3-aminopropyl) triethoxysilane (APTES), dimethylformamide (DMF), 1-ethyl-3-(3-dimethylaminopropyl) carbodiimide hydrochloride (EDC·HCl), N-hydroxysuccinimide (NHS), phosphate buffered saline (PBS), NH$_2$-PEG-COOH (average MW=2000), triethylamine, dimethyl sulfoxide (DMSO) and folic acid (FA) were purchased from Aladdin reagent Co. (http://www.aladdin-e.com, China). MCF-7 and A549 cells were made available from Guangdong Medical Laboratory Animal Center (http://gdmlac.com.cn, China).

Characterizations

The size and morphology of $Zn_{1.1}Ga_{1.8}Sn_{0.1}O_4$ nanoparticles were characterized using a field emission scanning electron microscopy (FE-SEM), Nova NanoSEM 430 (http://www.fei.com) equipped with an energy-dispersive X-ray (EDS), Model Inca 350 spectrometer, transmission electron microscopy (TEM) and high-resolution transmission electron microscopy (HRTEM), JEOL JEM-2100F microscope, operating at an accelerating voltage of 200 kV (http://www.jeol.com). For the irregular objects, the size of nanoparticles was defined as the biggest diameter in different directions. The crystalline structures were characterized by X-ray diffraction (XRD), Bruker AXS D8 Advance, in the scanning range of 15–65° using Cu/$K\alpha$ radiation as a source power (http://www.bruker.com). The size and Zeta potentials of the nanoparticles were characterized by Malvin Nano ZS90 (http://www.malvern.com). Photoluminescence (PL), photoluminescence excitation (PLE) and afterglow spectra, and decay curves were measured with a high-resolution spectrofluorometer (Edinburgh Instruments FLS920) equipped with a 500 W Xenon lamp (http://www.techcomp.com.hk). The chromo-photograph was taken by using the Canon Digital Single Lens Reflex (http://www.canon.com), while the NIR afterglow imaging were performed with a home-made imaging system including Germany pco dicam pro camera as the signal collector (http://www.pco-tech.com). Super-cold filters (Asahi, ZSC1100), long-pass filters (Asahi, ZVL630), and band-pass filters (Asahi, ZBPB147) were inserted to block the weak disturbance light and transmit the emission light (http://www.asahi-spectra.com). The images were analyzed with home-made imaging software. FT-IR spectra (Fourier transform infrared spectroscopy) were tested with a NICOTCT Fourier transform infrared spectroscopy (http://www.thermoscientific.com), while TGA (Thermal gravity analysis) was carried out with a Pyris 1 TGA thermogravimetric analyzer (http://www.perkinelmer.com).

Synthesis of $Zn_{1.1}Ga_{1.8}Sn_{0.1}O_4$: Cr^{3+} nanoparticles

$Zn_{1.1}Ga_{1.8}Sn_{0.1}O_4$: Cr^{3+} nanoparticles were synthesized according to a sol–gel method with small modification. $Zn(CH_3COOH)_2$, $SnCl_4$, $Ga(NO_3)_3$, $Cr(NO_3)_3$ and citric acid were dissolved in ultrapure water. The starting aqueous solutions of Zn^{2+}, Sn^{4+}, Ga^{3+} and Cr^{3+} were mixed according to the chemical formula of $Zn_{1.1}Ga_{1.8}Sn_{0.1}O_4$: Cr^{3+}. During the mixture, citric acid was last and slowly added with the molar ratio of total metal ions to citric acid 1:2, along with the addition of ammonia hydroxide to adjust pH to 3. The final solution was vigorously stirred at room temperature for 2 h, and then heated in an oven at 80 °C for 24 h. When the solution became a gel, n-butyl alcohol was added. The mixture was heated in an oil bath pan at 93 °C for 2 h, then heating up to 130 °C. After 1 h, the n-butyl alcohol treated gel was dried in an oven at 130 °C for 24 h. Finally, the obtained materials were annealed in air at 1100 °C for 1 h.

Surface Functionalization of FA-$Zn_{1.1}Ga_{1.8}Sn_{0.1}O_4$: Cr^{3+}

The synthesis of FA-ZGSC was modified from several previous publications [2, 10, 26], as shown in Scheme 1. The sintered ZGSC powders were ground for 30 min first, and then centrifuged at 10,000 rpm for 30 min to remove large size particles, and the supernatant was centrifuged at 13,000 rpm for 5 min to collect the precipitate. 30 mg dry precipitate was wet ground in minimum ethanol for 30 min. The obtained sample was dispersed in 20 mM NaOH solution by sonication for 1 h, and then stirred for 24 h. Then the solution was dried in an oven at 130 °C for 24 h again. 20 mg hydroxylated precipitate was re-dispersed in 30 mL DMF by sonication, while 200 μl APTES was mixed into the solution under
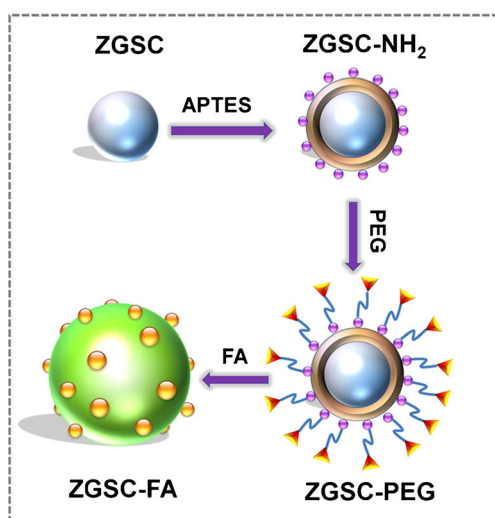
vigorous stirring at 80 °C for 24 h. The obtained amination-ZGSC was washed with DMF to remove unreacted APTES. 20 mg dried amination-ZGSC and 100 mg PEG were dispersed in 0.3 M PBS by sonication, and stirred for 24 h in dark at room temperature. The superfluous PEG were washed and removed by centrifugation three times with PBS. To conjugate FA with PEG-ZGSC, 1 mmol FA, 1.2 mmol EDC, 1.2 mmol NHS and 5 mmol triethylamine were dissolved in 20 mL anhydrous DMSO, and stirred for 4 h at room temperature. Then the solution was slowly poured into the 0 °C cold ethanol. The mixture consisted of the yellow flocculent precipitate and cold ethanol was stored in refrigerator for 12 h. The mixture was centrifuged at 13,000 rpm for 5 min to collect the FA-NHS precipitate. At last, the dried 1 mmol PEG-ZGSC and 5 mmol FA-NHS were re-dispersed in 10 mL DMSO, and then stirred for 48 h at room temperature. The resulting FA-ZGSC was washed three times with DMSO, and then dried at 80 °C for 12 h.

In vitro cellular uptake

MCF-7 and A549 cells were seeded into 8-well chambered coverglass at a density of $1 \cdot 10^3$ mL^{-1}. After 24 h, the medium was transferred to the serum-free medium containing ZGSC or FA-ZGSC nanoparticles (5 mg mL^{-1}). After 1 h incubation, the cells were washed thrice with PBS and fixed with 4 % paraformaldehyde solution for 40 min. Finally, the fixed cells were observed by the home-made imaging system including Germany pco dicam pro camera as the signal collector.

In vitro cytotoxicity

In the cytotoxicity experiment, BMSCs (bone mesenchymal stem cells) were cultured in HDMEM medium (Invitrogen, USA) containing 10 % heat-inactivated FBS (fetal bovine serum) at 37 °C in the humidified atmosphere with 5 % CO_2. The cells were seeded in 96-well plates at a density of $10 \cdot 10^3$ cells cm^{-2} and grew overnight prior to studies. Then, the cells were incubated with fresh media with FA-ZGSC (from 0.1 to 1000 mg cm^{-2}). After incubation for 3 days, 20 mL of MTT (thiazolyl blue tetrazolium bromide, 10 mg mL^{-1}, Sigma–Aldrich, USA) solution was added to each well of the plate, and then the plate was incubated at 37 °C for 4 h. Finally, the cells were lysed using DMSO (Sigma, USA). A microplate reader (Bio-Rad 680, USA) was applied to monitor the absorbance of the supernatants at 495 nm. This experiment was repeated for three times.

Results and discussions

The preparation process of FA-ZGSC nanoparticle is illustrated in Scheme 1. The ZGSC nanoparticles were synthesized by

**Scheme 1** Schematic illustration for the synthesis of FA-ZGSC nanoparticles

using the modified sol–gel method. Comparing to the previous method, the addition of n-butyl alcohol is utilized to improve the interaction between hydrogen bond and hydroxyl. The ZGSC nanoparticles via this method have been coated with a layer of n-butyl, which are beneficial to optimize the dispersibility. To improve the biocompatibility, colloidal stability and functionalization of targeting, the ZGSC nanoparticles were first ammoniated by coating APTES via a condensation reaction, and then PEGylated by adding the bifunctional NH_2-PEG-COOH. Further conjugation of the PEG-ZGSC with FA was carried out for tumor-targeted imaging application [26].

According to regular procedure, we first synthesize the ZGSC nanoparticles. The x-ray diffraction (XRD) pattern of ZGSC is similar to the spinel phase of $ZnGa_2O_4$ (JCPDS 38-1240) [22]. No peaks from other phases, such as ZnO, or Ga_2O_3 appear, indicating the formation of pure spinel phase zinc gallate (Fig. 1a). The analyses of size and morphology were performed by SEM and TEM (Fig. 1b–c). Though experiencing a higher sintered temperature, ZGSC nanoparticles still maintain the advantages of easy dispersibility, small-size (100±8 nm, 8 %), and some non-rod shape with different aspect ratios. DLS analysis further confirms the hydrodynamic diameter (~110 nm) of ZGSC nanoparticles (Fig. 1d). The HRTEM image demonstrated here was used to calculate the lattice spacing from lattice fringes (Fig. 1e) [2, 27]. The result (0.482 nm) corresponds to the d-spacing for the [111] crystal planes of the spinel. We performed the corresponding selected area electron diffraction (SAED) pattern with [001] zone axis (Fig. 1f). The well-defined diffraction spots confirm the face-

centered cubic-structured (fcc) (space group: Fd3m) single crystal [2].

The EDX spectrum of ZGSC nanoparticles show a significant signal of the Zn, Ga, Sn element, indicating that Sn has been incorporated into the spinel lattice structure (Fig. 2a). Besides the morphological study, we also conducted the spectroscopic measurement to identify the effectiveness of employing ZGSC nanoparticles as the nanoprobes with the operation waveband in the biologically transparent window. After being exposed under a Xenon lamp for 10 min, a long persistent luminescence with a broad emission band 600–850 nm, overlapping three sharp emission peaks at 688, 694 and 713 nm were detected (Fig. 2b). In order to identify which activator was taking part in the luminescent process, the excitation spectrum monitored at 694 nm of ZGSC during fluorescence was analyzed (Fig. 2c). The excitation spectrum consisted of three excitation bands, a stronger one centered about 254 nm and two weaker one around 430 and 583 nm, respectively. In view of the intensity differences, the former vests in the band-to-band transition, whereas the latter correspond to the crystal-field transitions, $^4A_2 \rightarrow {}^4T_1$ (t^2e) and $^4A_2 \rightarrow {}^4T_2$ (t^2e) of Cr^{3+} [27, 28]. The bright red to NIR fluorescence and long persistent phosphorescence were also visually evaluated by using a high resolution digital camera and supersensitive NIR camera in a dark room (Fig. 2d–e). The deep red photoluminescence can be discerned by bare eyes and captured by digital camera excited at 254 nm. The changes of NIR emission brightness with a decay time up to 6 h for these nanoparticles after being irradiated at 254 nm for 10 min show that ZGSC nanoparticles can be effectively

Fig. 1 ZGSC nanoparticles **a** XRD pattern; **b** SEM image; **c** TEM image; **d** DLS spectrum (PDI, 0.263); **e** HRTEM image; **f** SAED image
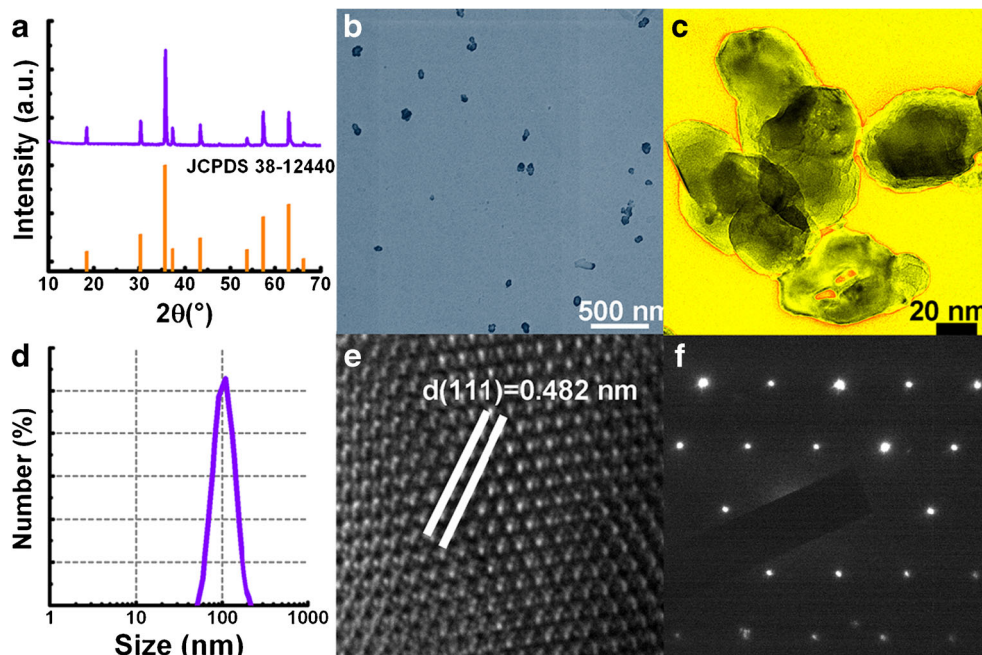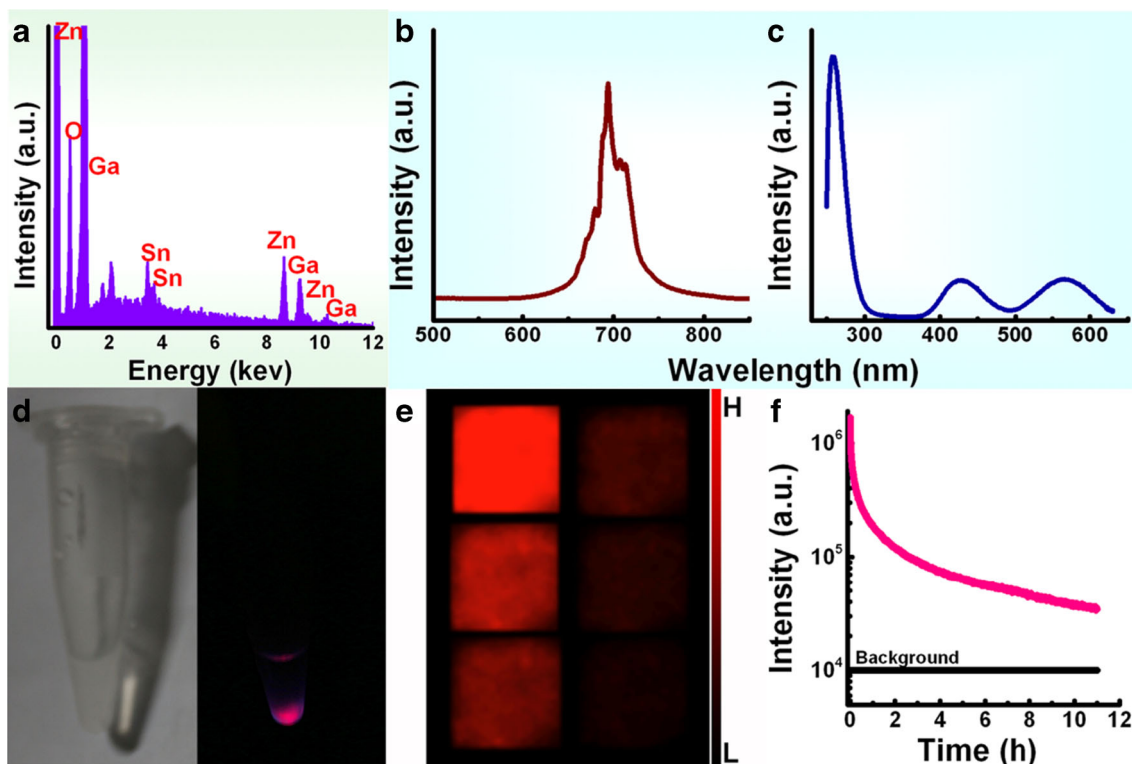
Fig. 2 ZGSC nanoparticles **a** EDX spectrum; **b** emission spectrum; **c** excitation spectrum; **d** photographs exposed under the sunlight illumination and 254 nm UV light; **e** NIR optical imaging taken at 1, 15, 45 min, 1.5, 3 and 6 h after the irradiation; (l) decay curves monitored at 694 nm. Before the measurements, the phosphors were annealed at 300 °C for 10 min and then pre-irradiated at 254 nm for 10 min

activated by UV light and result in 6 h of persistent NIR emission. The NIR emission decay of ZGSC after the irradiation for 10 min with a 254 nm UV lamp, demonstrates a fast decay at the beginning, and then a slow one, further confirming the excellent NIR afterglow properties with the longer persistent duration (>10 h, Fig. 2f).

To realize the functionalization for targeting, it is much essential to carry out a surface modification to ZGSC nanoparticles. Zeta potential, Fourier transform infrared (FT-IR) spectrometry and thermogravimetric analysis (TGA) were monitored to follow the functionalization [29]. Prior to any modification of the surface, hydroxyl groups were responsible for a negative zeta potential (−24.2 mV) of the core particle, due to the existence of many OH groups on the surface (Fig. 3a). After aminosilanization, all intermediates were characterized by a straight positive zeta potential 18.8 mV, due to the protonation of the amino groups at surface. Once the PEG layer coated the nanoparticle, zeta potential switched from positive to negative again (−29.1 mV), due to the presence of chain-end carboxyl groups on the surface. The similar variation is also observed by comparing the FT-IR spectra (Fig. 3b). The FT-IR spectra of amination-ZGSC main consisted of several characteristic strong absorption bands, including 1020 and 1134 cm^{-1} band, attributed to the stretching vibrations of O-Si-O [18], 2879 and 2945 cm^{-1} band, assigned to the asymmetric and symmetric CH_2-stretching bands [15], and 3288 cm^{-1} band, related to the N-H stretching bands [14]. These additional absorption bands successfully indicate the amination-modification of ZGSC nanoparticles. While more absorption bands at 1060 and 3450 cm^{-1} were shown in the FT-IR spectra of PEG-ZGSC. The former is assigned to the C-O bond and symmetric stretching vibrations of the C − H bond in PEG [8], and the latter was attributed to stretching vibration of C = O and the N − H bending mode of amino group in bifunctional PEG [15]. After conjugation with FA, the FA-ZGSC nanoparticle had some new intensity absorption peaks at 1519, and 2927 cm^{-1}, which were assigned to the stretching vibration of the phenyl, and the characteristic alkyl (R-CH_2) stretch vibration in FA, respectively [30]. These two bands also further confirm the successful FA-conjugation. The quantity of the conjugated FA can be evaluated according to TGA result from the weight loss between 30 and 600 °C (Fig. 3c). A slight weight loss below 150 °C was detected in the TGA curves of amination-ZGSC and FA-ZGSC, due to the loss of absorbed water. The sharp drop of weight for FA-ZGSC occurred in the 200–800 °C mainly contributes to the pyrolysis of PEG, the disappearance of FA and parts of APTES. Based on the above facts, it is suggested that FA has been successfully conjugated in FA-ZGSC nanoparticles.
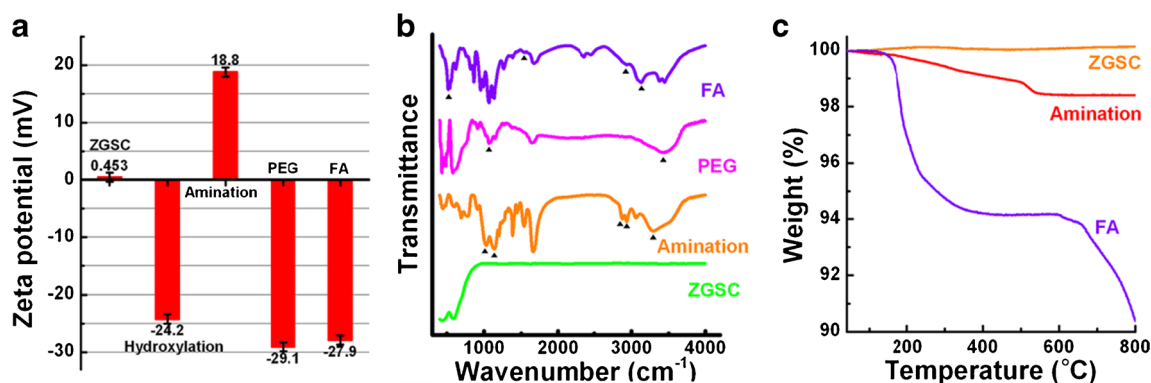
Fig. 3 Surface functionalization of FA-ZGSC **a** Zeta potential of unmodified ZGSC, hydroxylation-ZGSC, amination-ZGSC, PEG-ZGSC and FA-ZGSC; **b** FT-IR spectra of unmodified ZGSC, amination-ZGSC, PEG-ZGSC and FA-ZGSC; **c** TGA curves of unmodified ZGSC, amination-ZGSC and FA-ZGSC

After accomplishing the surface functionalization, it is very necessary to re-recognize the morphological and spectroscopic characteristic of FA-ZGSC nanoparticles. Figure 4a showed the SEM image of FA-ZGSC nanoparticles. FA-ZGSC nanoparticles presented more consistent cubic shape. Therefore, these surface modification agents are beneficial to not only stabilize the FA ligand, but also modify the surface feature. It is notable that the size of FA-ZGSC increased after accomplishing the surface functionalization, because FA was successfully loaded onto the surface of the ZGSC. DLS spectrum also further confirms this variation. The average diameter has increased to 220 nm (Fig. 4b). We also take the measurements to investigate the optical properties of FA-ZGSC nanoparticles after accomplishing the surface functionalization. As demonstrated in Fig. 4c–d, in addition to the same NIR emission bands originating from Cr^{3+} transition, an additional emission band in the visible region was also detected. The intense eye-visible nattier blue light can be
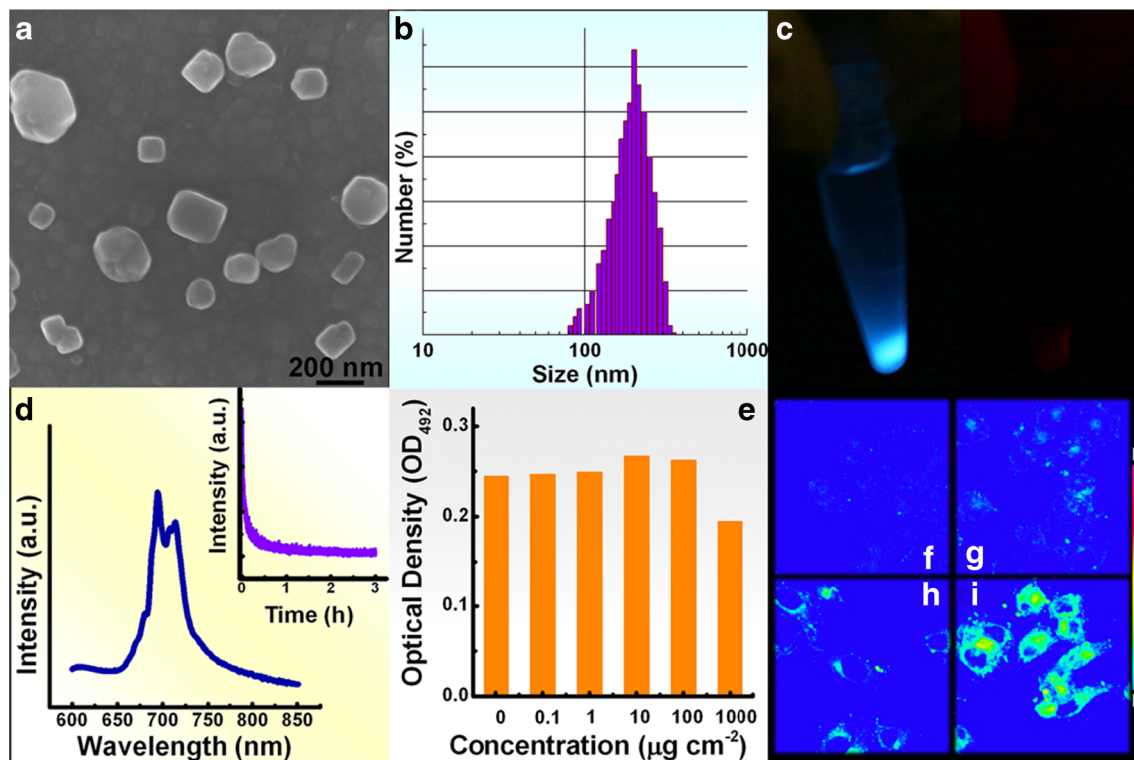

Fig. 4 FA-ZGSC nanoparticles **a** SEM image; **b** DLS spectrum (PDI, 0.224); **c** the digital photo under 254 nm UV excitation before and after inserting the 590 nm longpass filter. **d** photoluminescence spectrum. The inset shows the decay curves monitored at 694 nm. Before the measurements, the phosphors were annealed at 300 °C for 10 min and then pre-irradiated at 254 nm for 10 min; **e** in vitro cell viability incubated with FA-ZGSC. (**f**)–(**i**) in vitro cellular uptake and tumor cell imaging of ZGSC and FA-ZGSC. NIR images show FR positive human breast cancer cell line MCF-7 (*right*, **g** and **i**) and FR negative human lung cancer cell line A549 (*left*, **f** and **h**) uptake of ZGSC (*upside*, **f**–**g**) and FA-ZGSC (*underside*, **h**–**i**) after 1 h incubation

observed when excited at 254 nm, but when inserting a 590 nm longpass filter, the red photoluminescence reappear again. Considering the surface modification, the additional visible emission band may be assigned to singlet–singlet electronic transitions of organic molecule in FA [17]. We also evaluate the afterglow decay curve of FA-ZGSC nanoparticles (inset of Fig. 4d). Due to the surface coating of organic ligands, the afterglow intensity and persistent duration of FA-ZGSC nanoparticles both decrease. Seemingly, the organic coating acts as quencher of afterglow, leading to a noteworthy degradation of afterglow initial emission intensity and persistent duration. But 3 h of persistent duration can still ensure the potential application of advanced optical imaging with high resolution and weak light disturbance [31–33]. Cell viability and biocompatibility were tested via with the MTT kit. We observed cellular viabilities of greater than 95 % in the presence of injections with a concentration of ≤100 mg cm^{-2} (Fig. 4e), indicating relatively low toxicity of the employed nanoparticles. The cancer cell targeting ability was investigated by incubating the MCF-7 cell and A549 cell with ZGSC and FA-ZGSC nanoparticles (Fig. 4f–i). MCF-7 cells (known to overexpressing FR), and A549 cells (low FR expressing) were incubated with the same concentration of the ZGSC and FA-ZGSC for the same time. The internalization of nanoparticles incubated for 1 h was visualized by highly sensitive optical camera. Figure 4f–i demonstrated that MCF-7 cells (i) incubated with FA-ZGSC were much brighter than the A549 cells (h) incubated with the same materials. In addition, MCF-7 cells (g) and A549 cells (f) incubated with ZGSC under the same conditions showed no specific uptake optical property. These results indicated that the MCF-7 cancer cells were effectively internalized the FA-conjugated nanoparticles. Further researches covering the complete medical experiments towards the visualization of the structural and functional processes in tissues and in vivo, are still in progress.

Conclusions

Here, we successfully synthesized the FA-conjugated $Zn_{1.1}Ga_{1.8}Sn_{0.1}O_4$: Cr^{3+} nanoparticles with NIR long persistent phosphorescence for targeted fluorescence imaging of cancer cells by the modified sol–gel method. $Zn_{1.1}Ga_{1.8}Sn_{0.1}O_4$ nanoparticles showed the easy dispersibility, small-size, good crystallinity, and remarkable long persistent luminescence over 10 h in the near-infrared region. The surface modification of ZGSC by coating the activated functional group of NH_2, PEG and FA, ensures the functionalized targeted imaging. The functionalized nanoparticles have exhibited highly selective tumor localization, and caused an enabling long-term, real-time, reliable deep-tissues/cell/in vivo imaging with high resolution and signal to noise ratio.

References

1. Ahmed E, Morton SW, Hammond PT, Swager TM (2013) Fluorescent multiblock pi-conjugated polymer nanoparticles for in vivo tumor targeting. Adv Mater 25:4504–4510
2. Abdukayum A, Chen JT, Zhao Q, Yan XP (2013) Functional near infrared-emitting Cr^{3+}/Pr^{3+} co-doped zinc gallogermanate persistent luminescent nanoparticles with superlong afterglow for in vivo targeted bioimaging. J Am Chem Soc 135:14125–14133
3. Chen C, Ke J, Zhou XE, Yi W, Brunzelle JS, Li J, Yong EL, Xu HE, Melcher K (2013) Structural basis for molecular recognition of folic acid by folate receptors. Nature 500:486–489
4. Huang P, Bao L, Zhang C, Lin J, Luo T, Yang D, He M, Li Z, Gao G, Gao B, Fu S, Cui D (2011) Folic acid-conjugated silica-modified gold nanorods for X-ray/CT imaging-guided dual-mode radiation and photo-thermal therapy. Biomaterials 32:9796–9809
5. Pan J, Feng SS (2009) Targeting and imaging cancer cells by folate-decorated, quantum dots (QDs)- loaded nanoparticles of biodegradable polymers. Biomaterials 30:1176–1183
6. Chen L, Han H (2014) Recent advances in the use of near-infrared quantum dots as optical probes for bioanalytical, imaging and solar cell application. Microchim Acta 181:1485–1495
7. Zheng C, Zheng M, Gong P, Jia D, Zhang P, Shi B, Sheng Z, Ma Y, Cai L (2012) Indocyanine green-loaded biodegradable tumor targeting nanoprobes for in vitro and in vivo imaging. Biomaterials 33:5603–5609
8. Gabizon A, Horowitz AT, Goren D, Tzemach D, Shmeeda H, Zalipsky S (2003) In vivo fate of folate-targeted polyethylene-glycol liposomes in tumor-bearing mice. Clin Cancer Res 9:6551–6559
9. Yi Z, Zeng S, Lu W, Wang H, Rao L, Liu H, Hao J (2014) Synergistic dual-modality in vivo upconversion luminescence/X-ray imaging and tracking of amine-functionalized $NaYbF_4$:Er nanoprobes. ACS Appl Mater Interfaces 6:3839–3846
10. Maldiney T, Richard C, Seguin J, Wattier N, Bessodes M, Scherman D (2011) Effect of core diameter, surface coating, and PEG chain length on the biodistribution of persistent luminescence nanoparticles in mice. ACS Nano 5:854–862
11. Yoo MK, Park IK, Lim HT, Lee SJ, Jiang HL, Kim YK, Choi YJ, Cho MH, Cho CS (2012) Folate-PEG-superparamagnetic iron oxide nanoparticles for lung cancer imaging. Acta Biomater 8:3005–3013
12. Shin SJ, Beech JR, Kelly KA (2013) Targeted nanoparticles in imaging: paving the way for personalized medicine in the battle against cancer. Integr Biol (Camb) 5:29–42
13. Yang Y (2014) Upconversion nanophosphors for use in bioimaging, therapy, drug delivery and bioassays. Microchim Acta 181:263–294
14. Xia HX, Yang XQ, Song J-T, Chen J, Zhang MZ, Yan DM, Zhang L, Qin MY, Bai LY, Zhao YD, Ma ZY (2014) Folic acid-conjugated silica-coated gold nanorods and quantum dots for dual-modality CT and fluorescence imaging and photothermal therapy. J Mater Chem B 2:1945–1953
15. Fischer CR, Groehn V, Reber J, Schibli R, Ametamey SM, Müller C (2013) Improved PET imaging of tumors in mice using a novel (18) F-folate conjugate with an albumin-binding entity. Mol Imaging Biol 15:649–654

16. Sun L, Wei Z, Chen H, Liu J, Guo J, Cao M, Wen T, Shi L (2014) Folic acid-functionalized up-conversion nanoparticles: toxicity studies in vivo and in vitro and targeted imaging applications. Nanoscale 6:8878–8883

17. Pan YJ, Li D, Jin S, Wei C, Wu KY, Guo J, Wang CC (2013) Folate-conjugated poly(N-(2-hydroxypropyl)methacrylamide-co-methacrylic acid) nanohydrogels with pH/redox dual-stimuli response for controlled drug release. Polym Chem 4:3545–3553

18. Ye C, Wang YQ, Li CG, Yu J, Hu YZ (2014) Preparation of liposomes loaded with quantum dots, fluorescence resonance energy transfer studies, and near-infrared in-vivo imaging of mouse tissue. Microchim Acta 180:117–125

19. Bessière A, Sharma SK, Basavaraju N, Priolkar KR, Binet L, Viana B, Bos AJJ, Maldiney T, Richard C, Scherman D, Gourier D (2014) Storage of visible light for long-lasting phosphorescence in chromium-doped zinc gallate. Chem Mater 26:1365–1373

20. Maldiney T, Byk G, Wattier N, Seguin J, Khandadash R, Bessodes M, Richard C, Scherman D (2012) Synthesis and functionalization of persistent luminescence nanoparticles with small molecules and evaluation of their targeting ability. Int J Pharm 423:102–107

21. Li Y, Zhou S, Li Y, Sharafudeen K, Ma Z, Dong G, Peng M, Qiu J (2014) Long persistent and photo-stimulated luminescence in Cr^{3+}-doped Zn–Ga–Sn–O phosphors for deep and reproducible tissue imaging. J Mater Chem C 2:2657–2663

22. Sharma SK, Gourier D, Viana B, Maldiney T, Teston E, Scherman D, Richard C (2014) Persistent luminescence of AB_2O_4:Cr^{3+} (A=Zn, Mg, B=Ga, Al) spinels: New biomarkers for in vivo imaging. Opt Mater 36:1901–1906

23. Su Q, Li C, Wang J (2014) Some interesting phenomena in the study of rare earth long lasting phosphors. Opt Mater 36:1894–1900

24. Pan Z, Lu YY, Liu F (2012) Sunlight-activated long-persistent luminescence in the near-infrared from Cr^{3+}-doped zinc gallogermanates. Nat Mater 11:58–63

25. Li Y, Li YY, Sharafudeen K, Dong GP, Zhou SF, Ma ZJ, Peng MY, Qiu JR (2014) A strategy for developing near infrared long-persistent phosphors: taking MAlO3:Mn4+, Ge4+ (M=La, Gd) as an example. J Mater Chem C 2:2019–2027

26. Peng C, Qin J, Zhou B, Chen Q, Shen M, Zhu M, Lu X, Shi X (2013) Targeted tumor CT imaging using folic acid-modified PEGylated dendrimer-entrapped gold nanoparticles. Polym Chem 4:4412–4424

27. Maldiney T, Bessiere A, Seguin J, Teston E, Sharma SK, Viana B, Bos AJ, Dorenbos P, Bessodes M, Gourier D, Scherman D, Richard C (2014) The in vivo activation of persistent nanophosphors for optical imaging of vascularization, tumours and grafted cells. Nat Mater 13:418–426

28. Li Y, Du X, Sharafudeen K, Liao C, Qiu J (2014) A long persistent phosphor based on recombination centers originating from Zn imperfections. Spectrochim Acta A Mol Biomol Spectrosc 123:7–11

29. Sun L, Liu T, Qiu Y, Liu J, Li F, Shi L, Wolfbeis OS (2014) Direct formation of mesoporous upconverting nanoparticles for bioimaging of living cells. Microchim Acta 181:775–782

30. Müller C, Reber J, Schlup C, Leamon CP, Schibli R (2013) In vitro and in vivo evaluation of an innocuous drug cocktail to improve the quality of folic acid targeted nuclear imaging in preclinical research. Mol Pharm 10:967–974

31. Li Y, Zhou S, Dong G, Peng M, Wondraczek L, Qiu J (2014) Anti-stokes fluorescent probe with incoherent excitation. Sci Rep 4: 4059(1)–4059(6)

32. Van den Eeckhout K, Smet PF, Poelman D (2010) Persistent luminescence in Eu^{2+}-Doped compounds: a review. Materials (Basel) 3: 2536–2566

33. Zhuang Y, Ueda J, Tanabe S (2013) Tunable trap depth in Zn(Ga1−xAlx)2O4:Cr, Bi red persistent phosphors: considerations of high-temperature persistent luminescence and photostimulated persistent luminescence. J Mater Chem C 1: 7849–7855